Rev. Adv. Mater. Sci. 2019; 58:206–217

DE GRUYTER

Research Article

Hamid Reza Karimi Zarchi*, Ali Khajesarvi, Seyed Sadegh Ghasemi Banadkouki, and Mahesh C. Somani

Microstructural Evolution and Carbon Partitioning in Interstitial Free Weld Simulated API 5L X60 Steel

Abstract: The microstructural characterizations and partitioning of carbon element in the weld heat affected zones of a commercial API 5L X60 line pipe steel were studied by applying a high speed heating and cooling dilatometry technique in the present research work. The hollow cylindrical specimens were quickly heated to $1000°C$, soaked for only 5 s followed by continuous cooling to ambient temperature. Besides the construction of CCT diagram of this high strength low alloy steel using the dilatation data, the hardening response, microstructural features and carbon partitioning of weld simulated specimens were investigated. The obtained results showed that the hardening response of samples increased from 142 to $261 HV_{10kg}$ with increasing cooling rates. These hardening variations were attributed to the changes in microstructural features and carbon partitioning that occurred between the microconstituents present in the microstructures of weld simulated samples.

Keywords: Commercial X-60 line pipe steel; weld simulation; rapid heating and cooling dilatometry technique; carbon partitioning; construction of CCT diagram

*Corresponding Author: Hamid Reza Karimi Zarchi: Department of Mining and Metallurgical Engineering, Yazd University, University Blvd, Safayieh, Yazd, PO Box: 98195 − 741, Iran; Email: karimizarchi@yazd.ac.ir; Tel: +98 9132528680; Fax: +98 35 38210995
Ali Khajesarvi: Department of Mining and Metallurgical Engineering, Yazd University, University Blvd, Safayieh, Yazd, PO Box: 98195 − 741, Iran; Email: alikhajesarvi@stu.yazd.ac.ir
Seyed Sadegh Ghasemi Banadkouki: Department of Mining and Metallurgical Engineering, Yazd University, University Blvd, Safayieh, Yazd, PO Box: 98195 − 741, Iran; Email: sghasemi@yazd.ac.ir
Mahesh C. Somani: University of Oulu, Materials and Mechanical Engineering, Centre for Advanced Steels Research, Post Box 4200, 90014 Oulu, Finland; Email: mahesh.somani@oulu.fi

1 Introduction

Microalloyed high-strength low-alloy (HSLA) weldable steels have been developed over the last half-century and are widely used in applications such as offshore platforms, shipbuilding and the construction of pipelines for oil and gas transportation [1, 2]. Oil and gas pipelines are the high-pressure welded vessels, so safety and operational reliability are most important for these applications, especially for the high-pressure gas pipelines [3, 4]. The materials best suited for the requirements of oil and gas pipeline industry are interstitial free advanced high strength low alloy steels. Specifications regarding chemical composition, mechanical properties and other important issues like welding, cutting, manufacturing etc. for these materials are determined and standardized by American Petroleum Institute: API [5], International Organization for Standards: ISO [6] and other national agencies working in this field of research work. API standards are generally taken as the main references by many national agencies in order to set their own specifications for these materials and hence are accepted and popularly used worldwide. Some of the most important materials used in pipelines are various generations of X-grade microalloyed high-strength weldable steels [7−9], which are well specified according to API 5L standard [5]. The main features of these steels include high yield strength [10, 11], high toughness [12], good weldability [13] and low ductile-to-brittle transition temperature [14]. In order to further improve the weldability properties of these high strength steels, carbon content is usually kept low (≤0.1 wt.%) and the effect of reduction in strength and hardenability due to carbon reduction is compensated by adding manganese (between 1.4 to 1.9 wt.%) in addition to some minor amounts of strong carbide forming microalloyed elements such as Nb [15], Ti [16], V [17] and Mo [18]. These microalloyed elements, which lead to fine-grained microstructures, are responsible for simultaneous increase of strength, toughness and welding properties [19].

Table 1: Chemical composition of the investigated API 5L X-60 pipeline steel (in wt%).

Fe	C	Si	Mn	S	P	Mo	Nb	Ti	V	Ni	Cr	Al
Balance	0.070	0.250	1.660	0.006	0.013	0.120	0.066	0.022	0.033	0.021	0.021	0.027

Table 2: Various cooling rates and times (t8/5) applied by dilatometer in order to obtain the samples under different weld simulated conditions in conjunction with their associated samples' marks.

Sample mark	CC0.3	CC1	CC3	CC10	CC50	CC136	CC360
Cooling Rate ($^\circ$C/s)	0.3	1	3	10	50	136	360
Cooling time, t8/5 (s)	1000	300	100	30	6	2.2	0.8

Investigation of welded HSLA steel microstructures show various heat affected zones (HAZ) including coarse-grained heat affected zone (CGHAZ), fine grained heat affected zone (FGHAZ), and inter-critical heat affected zone (ICHAZ). These regions form adjacent to the weld deposit as a result of being heated to temperatures ≥1200, 900-1200 and 700-900°C, respectively [20]. In addition, a great deal of researches directed on the toughness of welded parts indicated that FGHAZ and ICHAZ are far more tougher than CGHAZ in welded parts [21, 22]. This is due to the formation of prior coarse-grained austenite [23] in the CGHAZ of welded steels, which subsequently transform to plate-like bainitic ferrite matrix associated with some martensite/austenite islands during cooling. The martensite/austenite islands in plate-like bainitic ferrite microstructures decrease the toughness of welded HSLA steels. Accordingly, grain refinement is the conventional method for improving the toughness of HAZ of these steels [24, 25]. Although the microstructure of pipeline microalloyed steels mainly consists of upper bainite in HAZ, the amounts of martensite/austenite islands in their microstructures are considered as the principal factor in controlling their toughness and weldability. On the other hand, the toughness of HAZ in weldable high strength steels is extremely dependent on the percentages of carbon and other alloying elements which are effectively present in the martensite/austenite islands.

The investigation of microstructures and mechanical properties of practical HAZ of welded parts, such as oil and gas steel pipelines, is very expensive and time-consuming. Therefore, it is necessary to similar weld situations by using various thermal simulations processes [26–29] and then evaluate the hardening variations in relation with the amounts of different microconstituents in order to anticipate the quality of welded steel pipelines. One of the most applied techniques used for weld simulation is rapid heating and cooling dilatation of steel samples [26–28].

In this research, the microstructural features in relation with the hardening variations and macrohardness property of API 5L X-60 steel extensively used as pipelines in the gas and petroleum industry was investigated under various cooling conditions by using a high-speed heating and cooling automatic dilatometer. Moreover, the volume fractions of different microconstituents and carbon redistribution in the weld simulated microstructures were evaluated.

2 Materials and Experimental Procedure

The chemical composition of API 5L X-60 pipeline steel used in this research work is presented in Table 1. A Theta-model high-speed heating and cooling dilatometer was used in order to investigate in detail the phase transformation and microstructural changes during continuous cooling of weld simulated samples. The hollow cylindrical specimens with the inner and outer diameters of 3.5 and 4.9 mm, respectively; and 13 mm height were used for dilatometry study. These samples were heated rapidly to 1000°C, soaked for 5s in the vacuum furnace at 1.32×10^{-7} atm (10^{-4} torr) and then cooled to ambient temperature at various cooling rates from 0.3 to 360°C/s by helium gas injection. The heat-treated samples under various cooling rates or times (t8/5) are listed in Table 2. Typical investigated samples were marked as CC0.3, CC1, CC3, CC10, CC50, CC136 and CC360 corresponding to the samples continuously cooled at 0.3, 1, 3, 10, 50, 136 and 360°C/s, respectively. The heat treatment cycles performed in this work are schematically shown in Figure 1. The mechanical grinding and polishing procedures were carried out according to ASTM E3 standard (http://www.astm.org/standard/E3.htm), and then the samples were etched with a 2% nital solution (2 ml
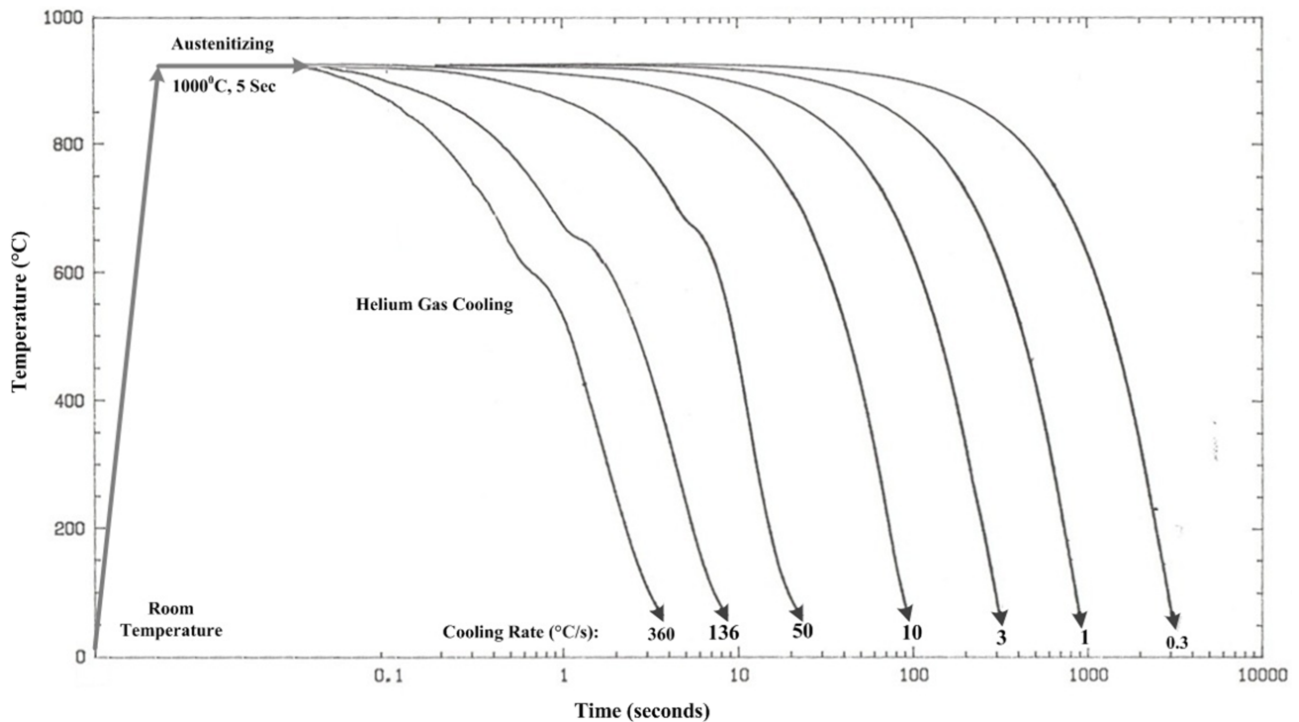
Figure 1: Schematic diagram of the heat treated cycles done by high-speed dilatometry on API X-60 samples in order to simulate weld simulation under different cooling rates.

HNO_3 and 98 ml C_2H_5OH) to reveal various microstructural features. Light and electron microscopic observations were carried out using an Olympus-PMG3 optical microscope and a TESCAN-MIRA 3 field-emission scanning electron microscope (FE-SEM), respectively. The micrographs were analyzed by image analyzing MIP software and the related volume fractions of different microconstituents were measured using the manual point count method according to the ASTM E 562 standard. In order to qualitatively investigate the carbon partitioning between the microconstituents, the spot-line scanning for carbon analysis was measured at various locations of polygonal ferrite, quasi-polygonal ferrite, degenerate pearlite, plate-like bainitic ferrite and martensite/austenite islands by using energy-dispersive X-ray spectroscopy (EDS) technique. The Vickers macrohardness measurements with a load of 10 kg (HV_{10kg}) were conducted on the weld simulated samples based on the ASTM E92 standard using an Instron Wolpert Gmbh-DLA 722 universal hardness tester.

3 Results and Discussion

3.1 Optical Microscopy and Hardness

Typical light micrographs taken from various weld simulated API X-60 samples are shown in Figure 2. The micrograph of CC0.3 samples (Figure 2a) indicates that the microstructure is mainly consisting of polygonal ferrite (light grains) with some carbide/ferrite dark contrasting regions called degenerate pearlite. It is interesting to point out that pearlite colony in plain carbon steels is a laminate microconstituent composed of alternating layers of ferrite and cementite formed by cooperative growth of these layers from prior austenite grain boundary at a relatively low cooling rate [30]; this is why degenerate pearlite might have formed by cementite nucleation at ferrite/prior austenite interfaces and then trapped with layers of ferrite in samples with very low carbon content under moderate cooling rates. Therefore, the degenerate pearlite formation in this sample is due to relatively slow cooling rate and very low carbon content (0.07%C). Further investigation of Figure 2a shows clearly that the polygonal ferrite grain boundaries are geometrically curved in the micrograph of CC0.3 sample. This is because of the reduction in carbon and iron diffusions due to the presence of considerable amounts of manganese and molybdenum elements in the alloy com-
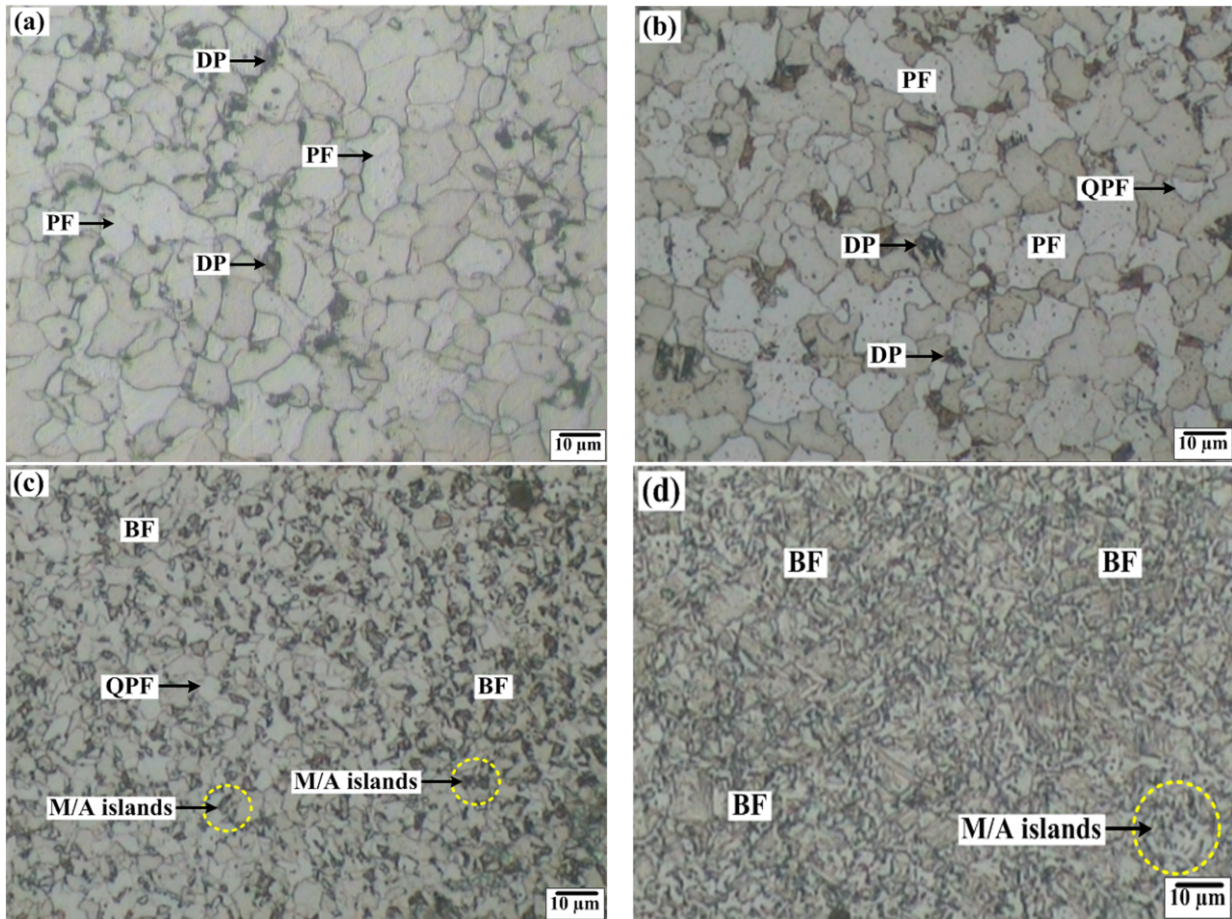
Figure 2: The light microstructures of various weld simulated API 5L X-60 pipeline steel samples under different cooling rates: (a) 0.3; (b) 10; (c) 50; and (d) 360°C/s. Degenerate pearlite, polygonal ferrite, quasi-polygonal ferrite, plate-like bainitic ferrite, and martensite/austenite island microconstituents are marked in the figures with DP, PF, QPF, BF, and M/A islands symbols, respectively.

position. In addition, the cooling rate of 0.3°C/s is so low that neither coarse nor fine laminate pearlite microphases can be formed and hence the degenerate pearlite forms instead. The micrograph of CC10 sample is presented in Figure 2b, indicating that the microstructure is mainly composed of the polygonal/quasi polygonal ferrite matrix and some dispersed degenerate pearlite. It is further observed that the ferrite grain boundaries are not completely continuum in the micrograph of CC10 sample in comparison with that of CC0.3 ones. Moreover, the amounts of grain boundary ferrite and degenerate pearlite have been increased while the matrix ferrite grains are also finer in micrograph of CC10 sample due to the higher cooling rate. The resultant microstructure of the samples cooled at 50°C/s (Figure 2c) is majorly composed of plate-like bainitic ferrite, associated with superimposed martensite/austenite islands and some quasi-polygonal ferrite. The ferrite matrix became finer and no evidence of degenerate pearlite formation was observed in these samples. With increasing cool-

ing rate, the volume fraction of polygonal ferrite decreased, while the blocks of martensite/austenite islands became finer and more elongated in the plate-like bainitic ferrite matrix. These results indicate that plate-like bainitic ferrite matrix with dispersed martensite/austenite islands have formed as a result of the mixed diffusional and shear phase transformation mechanisms. It is proposed that the plate-like bainitic ferrite forms at moderate cooling rates when the diffusion of carbon atoms from ferrite/prior austenite interface is relatively high but not sufficient enough for cementite nucleation and growth [31]. As a consequence of plate-like bainitic ferrite formation, the carbon content of prior austenite increases so that the austenite to bainitic ferrite phase transformation ceases and therefore the austenite is entrapped within the bainitic ferrite matrix. Such austenite entrapment results in the formation of islands consisting of martensite and/or retained austenite microconstituent in the plate-like bainitic ferrite microstructure. Increasing the cooling rate to 360°C/s (Fig-

ure 2d) causes the martensite/austenite islands to lose their blocky shape and become extremely fine and more elongated. Moreover, the plate-like bainitic ferrite is extensively observed in the needle-like form because of firstly the high cooling rates and secondly the decrease in carbon and iron diffusion rates.

For more comparison, the volume fractions of various microconstituents developed in the various weld simulated samples are listed in Table 2. The results show that the polygonal/quasi polygonal ferrite volume fraction decreased from 91.5 vol% in sample CC0.3 to 86 vol% in sample CC10 while the degenerate pearlite volume fraction increased from 8.5 to 14 vol%, respectively. The mentioned decrease in polygonal ferrite volume fraction in conjunction with increased degenerate pearlite formation are the reasons for the increase in the mean macrohardness from 142 to 191 HV_{10kg} in the samples cooled from 0.3 to 10°C/s (Figure 3). Further increase in cooling rate from 10 to 50°C/s, resulted in the activation of mixed shear and diffusional phase transformation mechanisms and converted some polygonal and quasi-polygonal ferrite to plate-like bainitic ferrite that was richer in carbon. As a result, the microstructure of the samples cooled at 50°C/s consists of martensite/austenite islands in plate-like bainitic ferrite matrix and has the higher mean macrohardness value of 215HV_{10kg}. Taking into consideration Figures 2c and 2d, it is clear that although it is not possible to measure the volume fraction of individual microconstituents present in the microstructure quantitatively but it is evident that more martensite/austenite islands have formed in the elongated plate-like bainitic ferrite matrix of CC360 sample in comparison with that of CC50 sample. As a result, the mean macrohardness measurement value for the CC360 sample is the highest and equals 261HV_{10kg} (Figure 3).
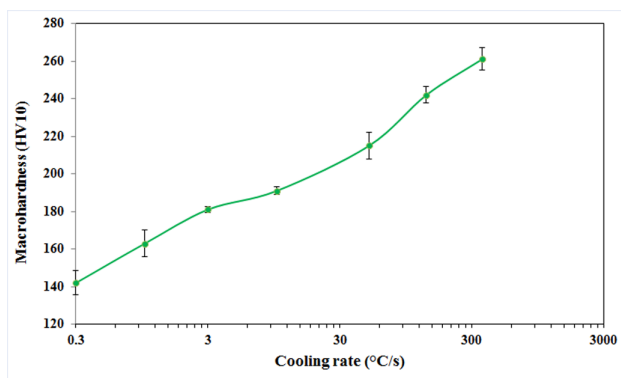

Figure 3: The macrohardness results of various weld simulated API 5L X-60 pipeline steel samples at different cooling rates. For information and better comparison, the macrohardness of raw API 5L X-60 steel samples in normalized condition is 173HV10kg.

3.2 Electron Micrographs and Carbon Partitioning

Figure 4 shows typical SEM micrographs in secondary electron mode taken from various weld simulated API X-60 samples. In comparison with the relevant light micrographs shown in Figure 2, the microconstituents including ferrite grains, degenerate pearlite, and plate-like bainitic ferrite associated with martensite/austenite islands are seen with a better contrasting resolution in the microstructures. These SEM micrographs confirm firstly that the plate-like bainitic ferrite has formed in the CC50 and CC360 samples (Figures 4b, 4c and 4d), while a mixture of polygonal and quasi polygonal ferrites has mainly formed with some degenerate pearlite in the CC0.3 and CC10 marked samples (Figures 4a and 4b). Secondly, the shape of plate-like bainitic ferrite crystals becomes more elongated and develops needle-like shape morphology with increasing cooling rate from 10 to 360°C/s as can be seen from the smaller sizes of martensite/austenite islands.

Since the austenite to ferrite phase transformation accompanies with redistribution of carbon in the prior austenite, the EDS spot-line scanning was extensively used within various microphases in order to investigate the level of carbon partitioning in the microstructures. In this regard, Figure 5 illustrates typical electron micrographs with superimposed EDS spot-line scanning for the carbon analysis, showing the variation of carbon concentration in terms of EDS numbers ($EDSN_S$) within the polygonal ferrite, degenerate pearlite, plate-like bainitic ferrite and martensite/austenite islands developed in different weld simulated samples. For more comparison, the EDS spot-line scanning results are also shown graphically in Figures 5a′ to 5d′. This is worth noting that although the EDS spot-line scanning technique for the carbon analysis cannot be used to measure the carbon concentration quantitatively and precisely, it has been used by several investigators to qualitatively compare the level of carbon contents of different microconstituents [32–34]. Careful investigation of Figure 5a′ shows that the carbon concentration was considerably reduced from degenerate pearlite (Ave.[1] = 9.31 EDSNs & S.D.[2] = 0.18) region to polygonal ferrite (Ave. = 4.33 EDSNs & S.D. = 1.66) in low cooled CC0.3 samples. Figure 5b′ also shows the same situation in CC10 samples for degenerate pearlite region whose average carbon concentration has been significantly increased to 13.25 EDSNs (S.D. = 2.40) while that of polygonal ferrite region is 6.11
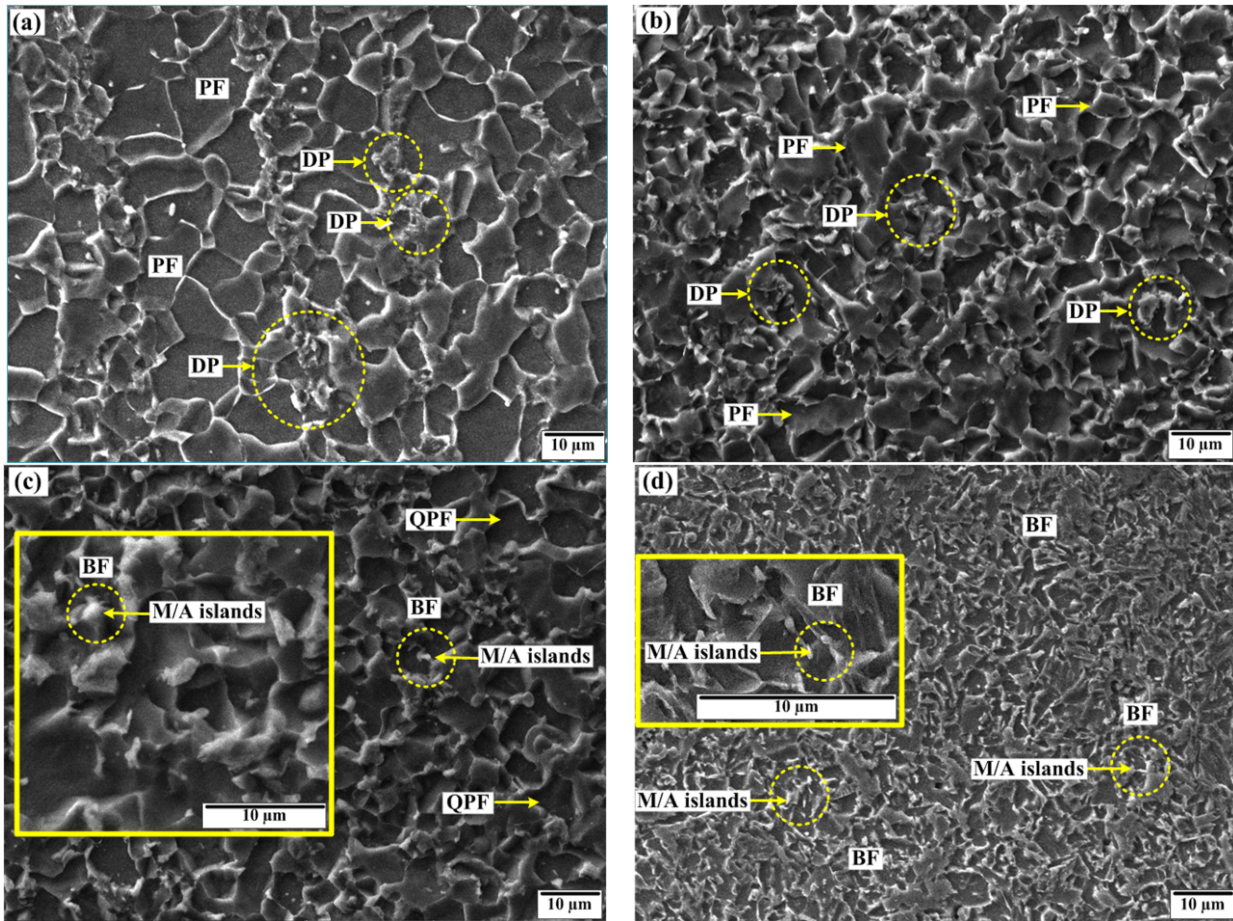
---

1 Average

2 Standard Deviation

Figure 4: SEM micrographs indicating the microstructural features of weld simulated API 5L X-60 pipeline steel samples under different cooling rates: (a) 0.3; (b) 10; (c) 50; and (d) 360°C/s. Degenerate pearlite, polygonal ferrite, quasi-polygonal ferrite, plate-like bainitic ferrite, and martensite/austenite island microconstituents are marked in the figures with DP, PF, QPF, BF, and M/A islands symbols, respectively.

EDSNs (S.D. = 1.12). This is due to the fact that the degenerate pearlite area contains some iron carbide which is enriched in carbon [30, 35]. Further investigation of both Figures 5a′ and Figure 5b′ shows that the EDS number of carbons decreased from the central region of polygonal ferrite grains to the vicinity of ferrite/austenite interfaces. This can be attributed to the low migration or diffusion rate of carbon from the more carbon-saturated central regions of polygonal ferrite formed at early stage of phase transformation in comparison to that of lateral ferrite area developed at the interfaces of ferrite/austenite areas. The low rate of carbon diffusion from central region toward the interfaces is because of the presence of considerable amounts of alloying elements including Si, Mn, and Mo in the steel composition. On the other hand, the carbon diffusion from the vicinity of polygonal ferrite grain into its ferrite/prior austenite interface is much faster because the polygonal ferrite crystals are less compact and have more lattice defects near the ferrite/prior austenite inter-

faces, causing the higher level of carbon redistribution and so more saturation in the regions nearby the prior austenite [36, 37]. Therefore, the degenerate pearlite is nucleated and grown from carbon-saturated ferrite/prior austenite in the faces. Another point can be extracted from further investigation of EDS spot-line scanning for carbon analysis is that the average carbon EDS number of polygonal ferrite has been increased from 4.33 EDSNs (S.D. = 1.66) of CC0.3 marked samples to 6.11 (S.D. = 1.12) for CC10 ones. This can be explained by significantly less amount of carbon rejection occurred from the polygonal ferrite in to the remaining prior austenite area during diffusional phase transformation at higher cooling rate of 10°C/s. Moreover, the carbon partitioning between plate-like bainitic ferrite and martensite/austenite islands formed in CC50 and CC360 samples are compared in Figures 5c′ and 5d′. In the first sight, it is observed that the average carbon EDSNs for martensite/austenite islands in CC50 marked samples is 12.25 EDSNs (S.D. = 0.81) while that one for bainitic ferrite
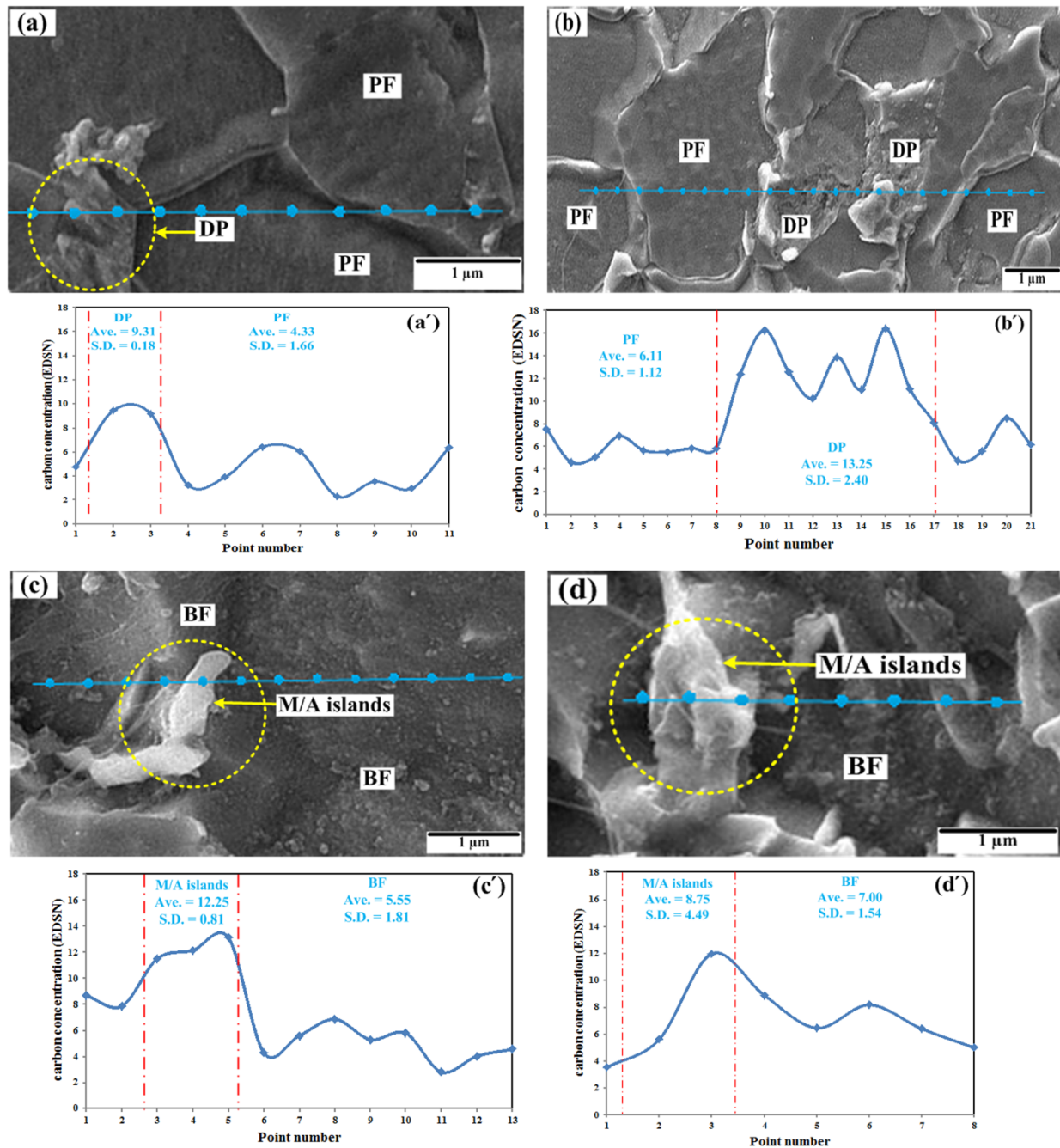
Figure 5: FE-SEM secondary electron micrographs with superimposed EDS spot-line scanning for the carbon analysis, showing the variation in the carbon concentration in terms of the EDS number (EDSNs) within the microconstituent observed in a and a') CC0.3 sample; b and b') CC10 sample; c and c') CC50 sample; and d and d') CC360 sample. The average (Ave.) of the EDS numbers for the carbon concentration with the corresponding standard deviation (S.D.) of the data points is indicated. DP: Degenerate Pearlite; PF: Polygonal Ferrite; BF: Plate-Like Bainitic Ferrite; and M/A islands: martensite/austenite island.
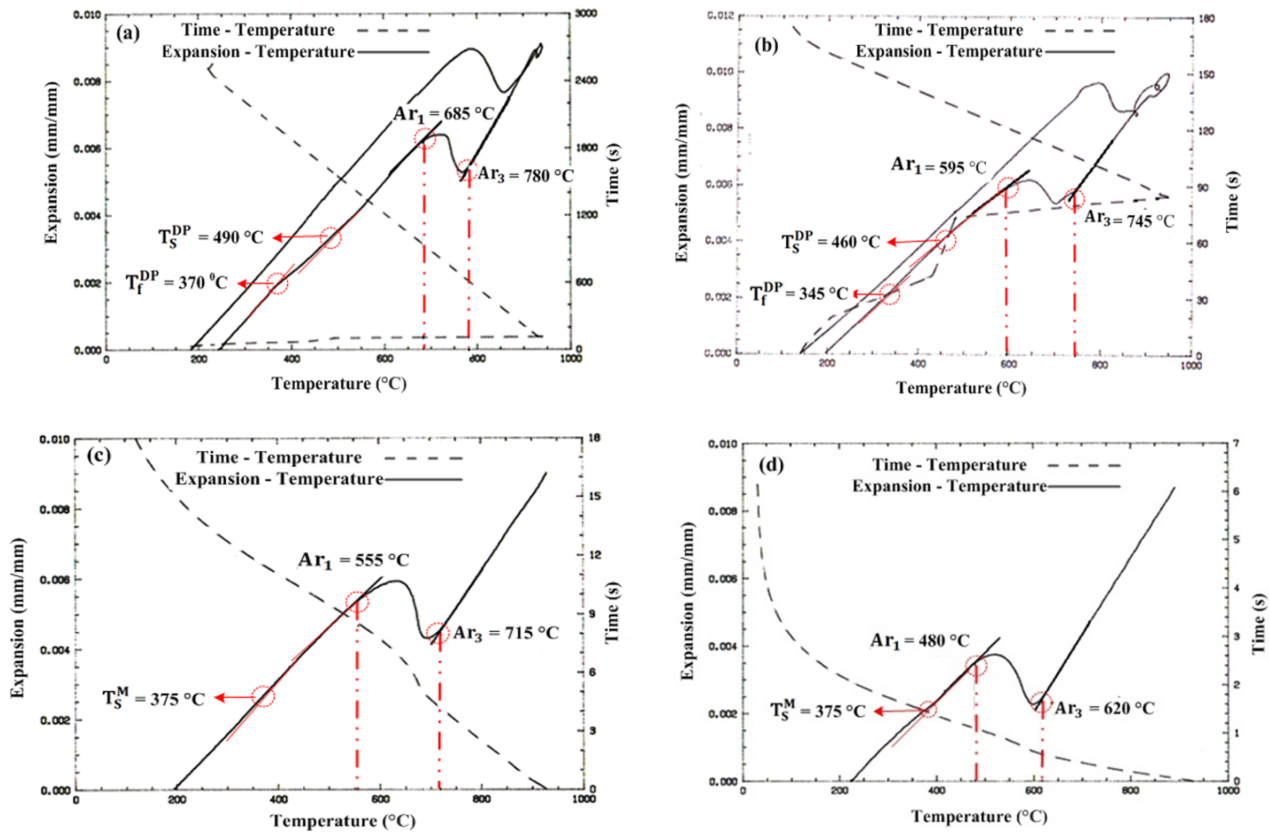
Figure 6: Dilation cooling curves of weld simulated API 5L X-60 pipeline steel at different cooling rates: (a) 0.3; (b) 10; (c) 50; and (d) 360°C/s. The dashed and solid lines represent Expansion – Time and Expansion – Temperature curves, respectively.

is 5.55 EDSNs (S.D. = 1.81). This means that the martensite/austenite islands held a significantly higher carbon concentration than that of bainitic ferrite. As already explained for the samples cooled at 0.3 and 10°C/s, the same situation existed here as well; *i.e.* when plate-like bainitic ferrite nucleated and grown from the prior austenite grain boundaries in the CC50 and CC360 marked samples, the carbon rejection from the bainitic ferrite into the prior austenite resulted in enhanced carbon saturation within the prior austenite and consequently these carbon enriched austenite areas consequently transformed to the martensite/austenite islands. On the other hand, when the average carbon EDSNs of martensite/austenite islands in CC360 samples (Ave. = 8.75 EDSNs & S.D. = 4.49) are compared with that of CC50 ones (Ave. = 12.25 EDSNs & S.D. = 0.81), it is observed that the carbon content of martensite/austenite islands has decreased significantly with the increase in cooling rate from 50 to 360°C/s due to the less amount of rejection of carbon from bainitic ferrite into the prior austenite areas. In addition, when the average EDSNs for plate-like bainitic ferrite in CC50 and CC360 samples are compared with those of polygonal ferrite formed in the

CC0.3 and CC10 samples, it is obviously seen that the carbon concentration of bainitic ferrite increased because of lesser times to diffuse from bainitic ferrite to the remaining austenite in the higher continuous cooled samples. This can be shown by the dilatation data (Figure 6) provided in Table 3. As is seen, the carbon diffusion and partitioning time between bainitic ferrite and remaining prior austenite has been decreased from seven to one second when the cooling rate has been increased from 50 to 360°C/s.

The experimented results show that the carbon concentration of martensite/austenite islands in CC50 samples are much higher than that of CC360 ones (Figures 5c′ and d′). This result shows that the carbon partitioning between different microconstituents has occurred which is quite variable during phase transformation even under rapid cooling rates of 50 and 360°C/s. On one hand, martensitic transformation start temperature depends on the concentration of carbon and other alloying elements present in the associated prior austenite areas. On the other hand, the carbon rejection to prior austenite has increased the carbon content of the austenite regions near to the prior austenite/bainitic ferrite interface in com-

Table 3: Volume fractions of the phases in the microstructures of weld simulated API 5L X-60 pipeline steel samples at different cooling rates.

Cooling rate ($^\circ$C/s)	**Cooling time, t8/5 (s)**	Degenerate pearlite volume fraction (%)	Polygonal or/and quasi polygonal ferrite volume fraction (%)	plate-like bainitic ferrite + martensite/austenite islands volume fraction (%)
0.3	1000	8.5	91.5	-
10	30	14	86	-
50	6	-	100*	
360	0.8	-	-	100

*the bainitic ferrite and the quasi polygonal ferrite cannot be distinguished from each other exactly.

Table 4: list of various phase transformation start temperature in association with the carbon partitioning time for enrichment into the remaining prior austenite in different weld simulated samples; the polygonal ferrite start temperature (Ar_3), the polygonal ferrite finish temperature (Ar_1), the degenerate pearlite start temperature (T_S^{DP}) and the degenerate pearlite finish temperature (T_f^{DP}).

Sample mark	Cooling time, t8/5 (s)	Ar_3 ($^\circ$C)	Ar_1 ($^\circ$C)	T_S^{DP} ($^\circ$C)	T_f^{DP} ($^\circ$C)	T_S^M ($^\circ$C)	Carbon diffusion time (s)
CC0.3	1000	780	685	490	370	-	1365
CC1	300	778	642	480	365	-	410
CC3	100	760	639	470	355	-	135
CC10	30	745	595	460	345	-	41
CC50		715	555	-	-	375	7
CC136		703	494	-	-	375	3
CC360		620	480	-	-	375	1

parison with the interior region of prior austenite. This causes the central regions of prior austenite to transform to martensite during cooling at a higher temperature, due to lower carbon content and hence the higher martensite start temperatures. In addition, the regions nearby to austenite/bainitic ferrite interfaces which have higher carbon content may be transformed to martensite with a relatively low temperature. In fact, during the martensite transformation in central regions of unstable prior austenite, the regions near to austenite interface remains untransformed and needs lower temperatures for martensite formation due to higher carbon content. Moreover, the high dislocation densities in the semi-stable austenite interface layer which are formed due to the high volumetric and martensitic-phase-transformation shear strains from the austenite central regions, help the interfacial austenite to get stable and, therefore further interfacial martensitic formation is ceased [38]. Eventually, the mentioned happenings result in the formation and dispersion of martensite/austenite islands in plate-like bainitic ferrite matrix in high cooled samples.

3.3 Weld Simulated CCT-Diagram

Typical Expansion-Temperature and Temperature-Time curves of various weld simulated API X-60 pipeline steel samples taken from a high-speed heating and cooling dilatometer are shown in Figure 6. As seen, all the curves drawn are cooled from 1000°C austenitizing temperature and their contraction-time dependence is linear to room temperature. This indicates that the slope change of dilatometry curves (length variation or expansion-temperature curves) has been related to the phase transformation due to the phase volume change. The investigation of dilatometry cooling curves for CC0.3 and CC10 samples shown in Figures 6a and 6b reveals that both of the samples have undergone a double stage phase transformation because of double line slope changes in these curves. The first slope change in Figure 6a, for the samples CC0.3 starts and finishes at 780 and 685°C and the second one at 490 and 370°C, respectively. While the first slope change for CC10 marked samples in Figure 6b, begins and ends at 745 and 595°C, and the second one at 460 and 345°C, respectively. Integrating these results with microscopic explanation mentioned in section (3.2), it can be clearly understood that the first and second stage of phase changes on dilatometric curves are related to ferrite (either polygo-
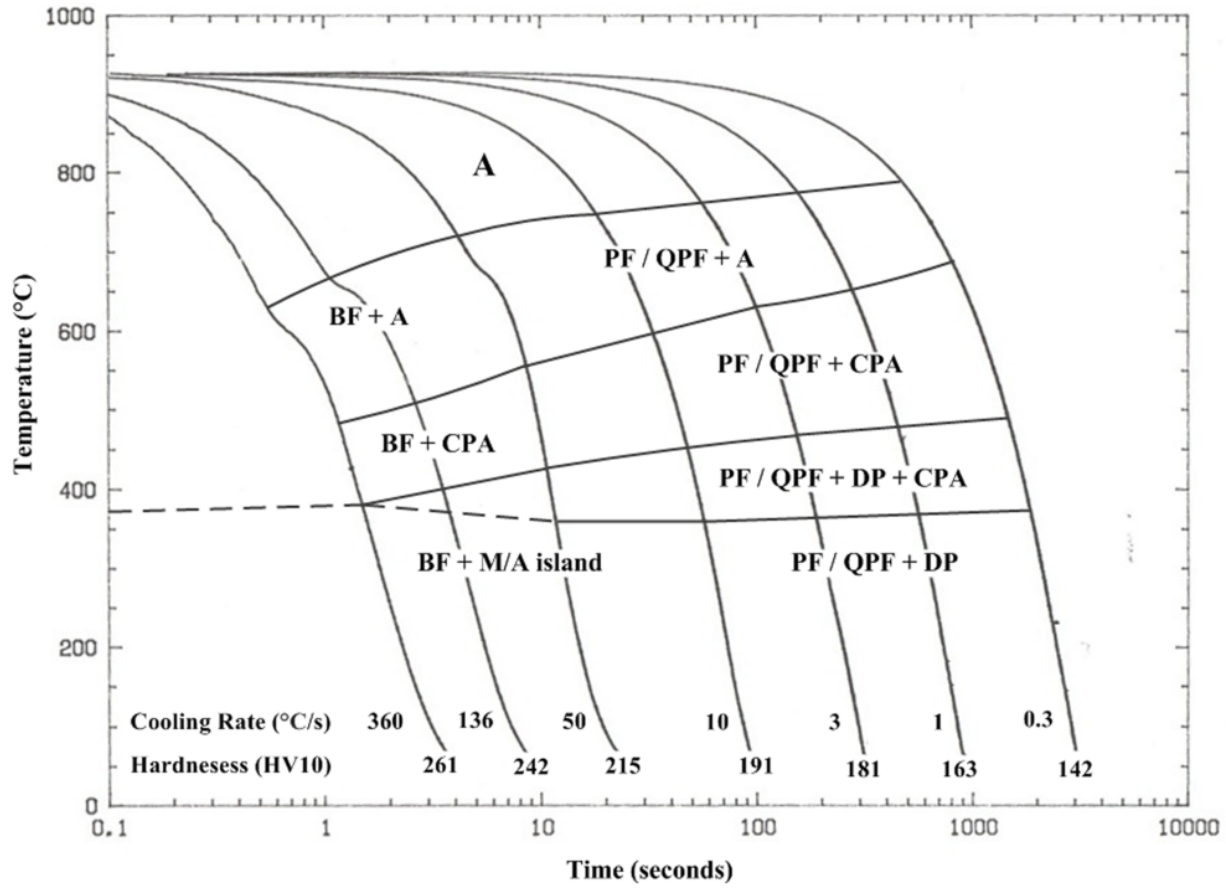
Figure 7: CCT diagram of API 5L X-60 pipeline steel for conditions of weld simulation. Pearlite, polygonal ferrite, quasi-polygonal ferrite, carbon partitioned austenite, plate-like bainitic ferrite and martensite/austenite island microconstituents are marked with P, PF, QPF, CPA, BF and M/A islands symbols, respectively.

nal or quasi-polygonal) and degenerate pearlite formation, respectively. Moreover, the results of Figure 6a show the carbon-saturated polygonal ferrite formation from prior austenite in CC0.3 sample started at 780°C (time 617 s) and finished during 321 seconds at 685°C (time 938 s). From this point afterwards the carbon-saturated polygonal ferrite and remaining prior austenite coexist and during further cooling till 490°C (time 1600 s), the carbon is rejected from polygonal ferrite and diffuses into the prior austenite making it richer in carbon and ready for transformation to degenerate pearlite. Then, the second phase change *i.e.* the degenerate pearlite formation begins at 490°C (time 1600 s) and ends during 380 s at 370°C (time 1980 s). The same situation exists for CC10 samples (Figure 6b). The carbon-rich polygonal and quasi-polygonal ferrite formation started at 745°C (time 108 s) during 14 s and finishes at 595°C while the degenerate pearlite was formed at 460°C (time 136 s) and completed at 345°C (time 149 s) in 13 seconds. Comparing the phase transformation temperatures of CC0.3 and CC10 samples (Table 3) including the polyg-

onal ferrite start temperature (Ar_3), the polygonal ferrite finish temperature (Ar_1), the degenerate pearlite start temperature T_S^{DP} and the degenerate pearlite finish temperature T_f^{DP} obviously shows they are shifted to lower temperatures due to increased cooling rate. In addition, considering the diffusion duration for carbon partitioning into prior austenite which starts at Ar_3 and finishes at T_f^{DP} indicates that the carbon diffusion time is decreased from 1365 s in CC0.3 to 41 s in CC10 samples (Table 3) resulting in higher carbon content of polygonal/quasi-polygonal ferrite formed in CC0.3 samples.

Two slop changes can also be seen on dilatometry cooling curves taken from 50 to 360°C/s weld simulated samples (Figures 6c and d) which are related to the plate-like bainitic ferrite and the martensite formations. Interpretation of these dilation results together with the microstructural features presented in part (3.2) demonstrates that the first slope change in Figure 6c curve is attributed to plate-like bainitic ferrite formation which starts at 715°C (time 4 s) and completes after 4 s at 555°C (time 8 s). The

second slope change is attributed to martensite formation which starts at 375°C (time 11 s). Accordingly, the investigation of Figure 6d indicates that the plate-like bainitic ferrite has formed in CC360 samples at 620°C (time 0.5 s) and finished only in 0.5 s at 480°C (time 1 s). From this point afterwards, further cooling down to 375°C (time 1.5 s), caused the carbon rejection from plate-like bainitic ferrite to prior austenite and making the central regions of remaining prior austenite ready for martensitic phase transformation. This figure clearly shows that the martensite formation starts in nearly 1.5 s after cooling from 1000°C austenitizing temperature. Based on these results, the continuous cooling transformation (CCT) diagram for API 5L X60 steel was drawn and presented in Figure 7 by using the data obtained from dilatometry cooling curves and the microstructural observations.

4 Conclusions

In the present research work, the microstructural evolution of weld simulated API 5L X-60 pipe line steel as well as the carbon partitioning in microphases were studied under various cooling rates by using a rapid heating and cooling dilatometry technique. Accordingly, the following conclusions were obtained:

1. The microstructure of weld simulated API X-60 steel at 0.3 cooling rate mainly consisted of 91.5 vol% polygonal ferrite and 8.5 vol% degenerate pearlite. Increasing the cooling rate to 10°C/s caused the decrease in polygonal/quasi polygonal ferrite volume fraction to 86 vol% and increase in degenerate pearlite volume fraction to 14 vol%. In addition, some quasi-polygonal ferrite also formed in the microstructures of weld simulated samples at 10°C/s.

2. The microstructures of weld simulated API X-60 steel at 50°C/s consisted of some quasi-polygonal ferrite and dispersed martensite/austenite islands in the plate-like bainitic ferrite matrix. Increasing the cooling rate to 360°C/s, caused the martensite/austenite islands to become finer and more elongated in the plate-like bainitic ferrite matrix, while the bainitic ferrite crystals became very fine and were observed in more needle-like form. In addition, the quasi-polygonal ferrite formation is omitted from the microstructure.

3. The mean macrohardness values of various weld simulated samples are increased from 142 to 261 HV_{10kg} by increasing the cooling rate from 0.3 to 360°C/s.

4. The increasing of cooling rate from 0.3 to 360°C/s causes the consequent appearance of polygonal ferrite, quasi-polygonal ferrite and plate-like bainitic ferrite formation in the microstructures. In addition, the average EDSNs carbon content of ferrite observed at 0.3 to 360°C/s cooling rates are increased from 4.33 to 8.75 EDSNs. This is due to lesser times for the rejection and diffusion of carbon element from saturated ferrite to the prior austenite with increasing of cooling rates.

5. The average carbon content of marensite/austenite islands is decreased from 12.25 to 8.75 EDSNs, by increasing of cooling rate from 50 to 360°C/s respectively. This is also due to the lesser carbon diffusion times from bainitic ferrite to prior remaining austenite which subsequently is transformed to martensite/austenite islands.

6. The CCT diagram of weld simulated API X-60 pipeline steel was constructed under various cooling rates by using the analysis of dilation data in conjunction with microstructural observations.

References

[1] A. Bahadori, Chapter 1 - Transportation pipelines, In: A. Bahadori (Ed.), Gulf Professional Publishing, Boston, 2017, pp. 1-27.

[2] X. D. Huo, J. Xia, L. J. Li, Z. W. Peng, S. J. Chen, and C.-T. Peng, Mater. Res. Express, 5(6) (2018) 062002.

[3] C. Zhuang, C. Huo, Y. Feng, In: 25th International Conference on Offshore Mechanics and Arctic Engineering, Hamburg, Germany, 2006, pp. 17-23.

[4] D.V. Lebedev, Met Sci Heat Treat, 19(7) (1977) 539-540.

[5] A.P. Institute, API Publishing Services, Washington, D.C., 2004, pp. 1-155.

[6] I.O.f. Standards, ISO 3183:2012, International Organization for Standards, 2012, pp. 179.

[7] M. Singh, R. Kumar, D. K. Shukla and K. S. Arora, Mater. Res. Express, 6(2) (2019) 026561.

[8] M. Witek, J. Nat. Gas. Sci. Eng., 27 (2015) 374-384.

[9] R. Hendi, H. Saifi, K. Belmokre, M. Ouadah, B. Smili, and B. Talhi, Mater. Res. Express, 5(3) (2018) 036523.

[10] H. G. Hillenbrand, A. Liessem, K. Biermann, C. J. Heckmann, and V. Schawinn, Proceeding of International Pipeline Conference, EUROPIPE, Calgary, Alberta, Canada, October 2004, pp. 1-7.

[11] S. S. Sohn, S. Y. Han, S. Y. Shin, J. -H. Bae, and S. Lee, Met. Mater. Int., 19(3) (2013) 377-388.

[12] A.K. Lis, J. Lis, and L. Jeziorski, J. Mater. Process. Technol., 64(1) (1997) 255-266.

[13] S. K. Sharma and S. Maheshwari, J Nat Gas Sci Eng, 38 (2017) 203-217.

[14] S. Kumar and S. K. Nath, J. Mater. Process. Technol., 236 (2016) 216-224.

[15] H. Tamehiro, M. Murata, R. Habu, and M. Nagumo, Trans. Iron Steel Inst. Jpn., 27(2) (1987) 120-129.

[16] B. Beidokhti, A. H. Koukabi, and A. Dolati, J. Mater. Process. Technol, 209(8) (2009) 4027-4035.

[17] L. Holappa, V. Ollilainen, W. Kasprzak, J. Mater. Process. Technol., 109(1) (2001) 78-82.

[18] T. Schambron, A. Dehghan-Manshadi, L. Chen, T. Gooch, C. Killmore, and E. Pereloma, Met. Mater. Int., 23(4) (2017) 778-787.

[19] J. R. Davis, Alloying: Understanding the Basics, ASM International, (2001).

[20] Z. Śloderbach and J. Pająk, Arch. Metall. Mater., 60(4) (2015) 2607-2612.

[21] K.S. Arora, S.R. Pandu, N. Shajan, P. Pathak, M. Shome, Int J Pres Ves Pip, 163 (2018) 36-44.

[22] Y. Terada, H. Tamehiro, H. Morimoto, T. Hara, E. Tsuru, H. Asahi, et al., In: 22nd International Conference on Offshore Mechanics and Arctic Engineering, The American Society of Mechanical Engineers, Mexico, 2003.

[23] S. Kumar, S.K. Nath, V. Kumar, Mater. Design, 90 (2016) 177-184.

[24] Y. Terada, A. Kojima, A. Kiyose, T. Nakashima, N. Doi, T. Hara, H. et al., In: 23rd International Conference on Offshore Mechanics and Arctic Engineering, The American Society of Mechanical Engineers, Canada, 2004, pp. 751-756.

[25] Y. Zhou, T. Jia, X. Zhang, Z. Liu, and R. D. K. Misra, J. Mater. Process. Technol., 219 (2015) 314-320.

[26] M. Shome, O.P. Gupta, O.N. Mohanty, Metall. Mater. Trans. A, 35(13) (2004) 985-996.

[27] T. Falkenreck, A. Kromm, and T. Böllinghaus, Weld. World, 62(1) (2018) 47-54.

[28] G. Spanos, R.W. Fonda, R.A. Vandermeer, and A. Matuszeski, Metall. Mater. Trans. A, 26(12) (1995) 3277-3293.

[29] Y. H. Guo, L. Li, X. M. Pan, D. H. Zhang, L. Lili, and M. K. Lei, Mater. Res. Express, 6(1) (2019) 016523.

[30] V.G. Vaks, A.Y. Stroev, V.N. Urtsev, and A.V. Shmakov, J. Exp. Theor. Phys., 112(6) (2011) 961-978.

[31] H.K.D.H. Bhadeshia, Bainite in Steels: Transformations, Microstructure and Properties, IOM Communications, 2001, pp. 19-61.

[32] A. Sabet Ghorabaei and S. S. Ghasemi Banadkouki, Mater. Sci. Eng. A, 700 (2017) 562-573.

[33] C. Y. Wang, J. Shi, W. Q. Cao, and H. Dong, Mater. Sci. Eng. A, 527(15) (2010) 3442-3449.

[34] S. S. Ghasemi Banadkouki and E. Fereiduni, Mater. Sci. Eng. A, 619 (2014) 129-136.

[35] Y. T. Chen and C. M. Zhu, In: Materials Science and Technology Conference, Association for Iron & Steel Technology, United States, 2009, pp. 1718-1728.

[36] J. Cermak and L. Kral, J. Alloy. Compd., 586 (2014) 129-135.

[37] A. Ebrahimian and S.S. Ghasemi Banadkouki, J. Alloy. Compd., 708 (2017) 43-54.

[38] M. Maalekian, E. Kozeschnik, S. Chatterjee, and H. Bhadeshia, Mater Sci Tech-Lond, 23(5) (2007) 610-612.